Contents list available at IJRED website

Int. Journal of Renewable Energy Development (IJRED)

Journal homepage: http://ejournal.undip.ac.id/index.php/ijred

Research Article

Numerical Study of Effect of Blade Twist Modifications on the Aerodynamic Performance of Wind Turbine

Wiroj Beabpimai[a] and Tawit Chitsomboon[b*]

[a]School of mechanical engineering, Institute of engineering, Suranaree University of Technology, Nakhonratchasima, Thailand

[b]Independent researcher, Nakhonratchasima, Thailand

ABSTRACT. This paper aims to investigate aerodynamic performance of a wind turbine blade with twist modifications using computational fluid dynamics (CFD). The phenomenon of 3D stall-delay effect in relation to blade twist is the key feature to be investigated in order to improve efficiency of a wind turbine. The NREL (National Renewable Energy Laboratory) Phase VI wind turbine rotor was used for validation and as the baseline rotor. The baseline blade geometry was modified by increasing/decreasing the twist angles in the inboard, mid-board and outboard regions of the blade in the form of a symmetrical curve with maximum twist angle of 3°. The steady incompressible Reynolds-averaged Navier-Stokes (RANS) equations with the k-ω Shear Stress Transport (SST) turbulence closure model were used for the calculations at wind speeds ranging from 5-20 m/s. The computational results for the baseline Phase VI rotor were validated against experimental data and a good agreement was found. The computational results for the modified blades were compared against those of the baseline blade. It was found that increase of annual energy production of up to 5.1% could be achieved by this modification technique.

Keywords: CFD, wind turbine, blade twist, stall delay, NREL Phase VI

Article History: Received: March 29, 2019; Revised: August 17, 2019; Accepted: August 19, 2019; Available online: Oct 30,2019
How to Cite This Article: Beabpimai, W., and Chitsomboon, T. (2019) Numerical Study of Effect of Blade Twist Modifications on the Aerodynamic Performance of Wind Turbine. Internasional Journal of Renewable Energy Development, 8(3), 285-292.
https://doi.org/10.14710/ijred.8.3.285-292

1. Introduction

Renewable and sustainable energies are increasingly being researched to provide the world with clean and reliable energy sources. Renewable energies can be used for various purposes with several applications such as electricity generation, desalination, cooling, heating, etc. Some interesting papers on solar and nanofluid can be found in references (Ahmadi et al., 2018(1)-(3), and Ramezanizadeh et al., 2019). Wind energy is another option which has experienced rapid growth during recent decades in terms of technology and commercialization. Research and development on making wind turbines to be more efficient and competitive are crucial. The rotor blades are very important parts of a wind turbine since they convert kinetic energy of the wind into mechanical power. Designing of wind turbine rotor blade to yield a high efficiency is a very challenging task since it involves various complicated aerodynamic manipulations.

Accurate predictions of aerodynamic forces are necessary for the effective design of wind turbine blades. Innovations are also needed to gain appreciable increase in efficiency. Generally, two main theoretical approaches for the design of wind turbine are the Blade Element Momentum (BEM) theory, and the Computational Fluid Dynamics (CFD). The BEM method is computationally fast and is easy to implement but has some limitations such as there is no inclusion of the three-dimensional (3D) effects and the unsteady effects (Hansen *et al.* 2006). On the other hand, the CFD method which employs the Navier-Stokes equations, does not have these limitations and thus can provide a deeper insight into the complex flow phenomena over wind turbine rotor. CFD methodology has been widely used in the literature to analyze the aerodynamic performance of horizontal-axis wind turbines (see, e.g., Sørensen *et al.* 2002; Johansen et al. 2002; Duque *et al.* 2003; Hsu *et al.* 2012; Li *et al.* 2012;).

Twist angle of a blade is one of key parameters in design, having considerable effects on the mechanical power capture of a wind turbine rotor. The twist angle is defined as the angle between the local airfoil chord and that at the blade tip. The increase in incidence angle of relative flow velocity from the blade tip to the root suggests that a blade be twisted more toward the root in order to achieve the optimal flow angles over the entire length of the blade. Most commercial wind turbines have nonlinear twist distributions along the blades. The twist angles toward the root are greater than the angles toward the tip. However, in the case of nonlinear blade twist distributions with increasing or decreasing twist angles at

* Corresponding author: tawit.boon@gmail.com

some regions of the blade span, the aerodynamic performances of rotor blade have not been extensively researched and only a few studies exist. Guntur (2013) numerically studied the MEXICO rotor with inboard twist modifications and found that the trailing vortices, which is caused by the change in the span-wise loading, results in an effect similar to that typically observed near the blade tip. Chow and van Dam (2012) investigated the effects of twist modifications in the inner area of the 5 MW rotor. The study focused on wind speed of 11m/s, at the knee of the power curve. The results showed that increasing inboard blade twist reduces rotor power capture and thrust. With decreasing inboard blade twist, rotor power remains constant while thrust increases approximately linearly.

3-D rotational effects on wind turbine blade is a very interesting phenomenon. It was found to delay stall at high angles of attack and increase lift coefficient significantly over that of 2-D airfoil, especially at the inboard region of the blade span. This behaviour is also referred to as stall-delay; it was first observed by Himmelskamp (1947) on propellers and was further investigated in several later studies, e.g. Wood (1991), Ronsten (1992), Schreck and Robinson (2002). This research proposes to investigate and explore beneficial effects of the 3-D stall by altering blade twists from that of the baseline values.

In this study, the effects of blade twist modifications on the aerodynamic performance of wind turbine rotor have been investigated using CFD methodology. The Phase VI wind turbine rotor of the National Renewable Energy Laboratory (NREL) was chosen as the baseline configuration. The baseline blade geometry was modified by increasing or decreasing the twist angles on three different regions along the blade span. The computational results of the modified blades were compared against those of the baseline blade, in terms of rotor power, thrust and annual energy production (AEP).

2. Methods

2.1 Specification of wind turbine rotor

The NREL Phase VI rotor shown in Figure 1 is a two-blade wind turbine with stall regulated design, which was tested comprehensively in the large wind tunnel of NASA Ames Research Center under extensive range of operating conditions (Hand et al. 2001). This wind turbine has a rotor radius of R=5.029 m and a power rating of 19.8 kilowatt (kW). The blade geometry is based on the S809 airfoil profile, with a nonlinear twist and a linear taper (Giguere and Selig 1999). The twist and chord distributions, and the geometric model of the blade are shown in Figure 2. The blade twists decrease from 20.04° at r/R=0.25 to -1.815° at the tip. The blade chords taper from 0.737 m at r/R=0.25 to 0.355 m at the tip. In the NREL Phase VI experimental campaign, an upwind configuration consisting of the cone angle of 0°, non-yaw, the tip pitch angle of 3° and the rotational rotor speed of 72 rpm, is considered for this computational study. More details about the wind turbine and procedures of the experiment are available in Hand et al. (2001).

Fig 1. NREL Phase VI wind turbine in the wind tunnel of NASA-Ames (Hand et al. 2001)

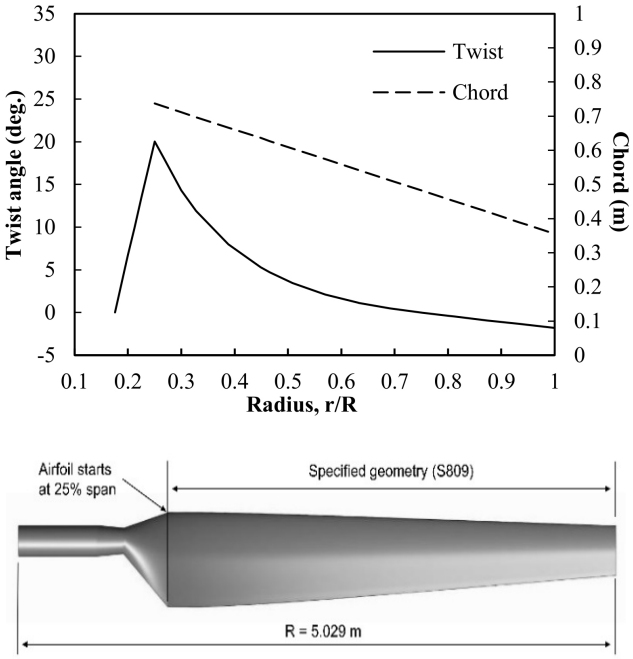

Fig 2. Geometry of the NREL Phase VI blade; chord and twist distributions, and top view of the blade

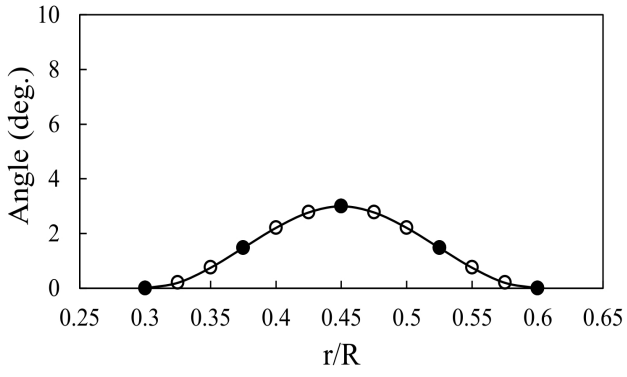

Fig 3. Designed blade twist distribution

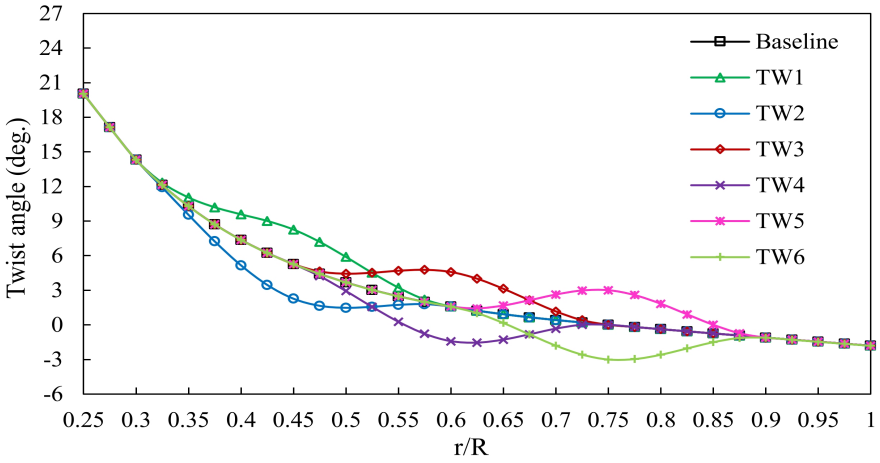

Fig 4. Spanwise twist distributions for the baseline and modified blades

2.2 Twist distribution modification

The blade was identical to that of the baseline NREL Phase VI, only the twist angles over a specific region of the blade were modified. An example of the twist angle distributions that were changed from the baseline blade was a symmetry curve with a maximum angle of 3° degree as shown in Fig.3. The curve was constructed by a cubic spline function through five control points (solid points in the figure). The starting and the ending points were set to be zero while the other three control points were determined by the Gaussian function (Eq. (1)).

$$G(x) = a\exp\left(-\frac{(x-b)^2}{2c^2}\right) \quad (1)$$

Where a, b, and c are constants

The numerical experiments were performed over the regions of blade spans: r=0.30-0.60R (TW1 and TW2), 0.45-0.75R (TW3 and TW4), and 0.60-0.90R (TW5 and TW6), with increasing or decreasing twist angles in each blade span. The final blade twist distributions along the blade span are shown in Figure 4.

2.3 Numerical method

The computational mesh is illustrated in Fig.5. The flow domain is semi-cylindrical geometry since the wind turbine contains two symmetrical blades. Therefore, only one of the two blades is modelled to save computational resources, and the remaining blade is accounted for using periodic boundary conditions imposed on the 180° cyclic boundaries. The computational domain extends the wind turbine six rotor radius upstream, five rotor radius in the span-wise direction, and eight rotor radius downstream to guarantee that the turbine flow is independent of the presence of the outer boundaries (Thumthae and Chitsomboon 2007).

For the inlet boundary condition, uniform velocity normal to the inflow surface with turbulence intensity of 0.5% was imposed. At the downstream outlet boundary, the pressure outlet condition was used. The wind tunnel wall was treated as a symmetry boundary condition. On the rotor blade surface, the no-slip wall condition was imposed. The wind speeds of the simulation were 5, 7, 9, 10, 11, 13, 15, 17, and 20 m/s with 1.23 kg/m^3 air density and 1.78^{-5} kg/(m.s) viscosity, for all of the runs.

The computational mesh generated by ANSYS ICEM CFD software (ANSYS ICEM CFD, 2009). The mesh contained about 2.74 million hexahedral cells based on grid independence tests. The grid was an O-type topology along most of the blade surface with 185 nodes around the airfoils and 165 nodes in the spanwise direction. The y^+ of the first cell layer close to the blade surface was around 1 with a growth ratio of 1.2 in order to ensure a well resolved boundary layer.

The CFD computation was performed with the commercial code ANSYS FLUENT (ANSYS FLUENT, 2009) which is based on the finite volume method. The steady, incompressible, Reynolds-averaged Navier-Stokes (RANS) equations were applied to solve the problem on a rotating reference frame. The QUICK scheme was used for discretization of convective term, and SIMPLE algorithm was used for pressure-velocity coupling. The iterative tolerances of convergence for all solved variables were set at 10^{-6}.

For turbulence modeling, the shear stress transport (SST) k-ω turbulence closure model (Menter et al. 2003) was selected because of its good predictions of boundary layer flows under adverse pressure gradient and separation. The formulation of the model is expressed below:

$$\frac{\partial(\rho k)}{\partial t} + \frac{\partial(\rho U_j k)}{\partial x_j} = \tilde{P}_k - \beta^* \rho k \omega + \frac{\partial}{\partial x_j}\left[(\mu + \sigma_k \mu_t)\frac{\partial k}{\partial x_j}\right] \quad (2)$$

$$\frac{\partial(\rho \omega)}{\partial t} + \frac{\partial(\rho U_j \omega)}{\partial x_j} = \alpha \rho S^2 - \beta \rho \omega^2 + \frac{\partial}{\partial x_j}\left[(\mu + \sigma_\omega \mu_t)\frac{\partial \omega}{\partial x_j}\right] + 2(1-F_1)\frac{\rho \sigma_{\omega 2}}{\omega}\frac{\partial k}{\partial x_j}\frac{\partial \omega}{\partial x_j} \quad (3)$$

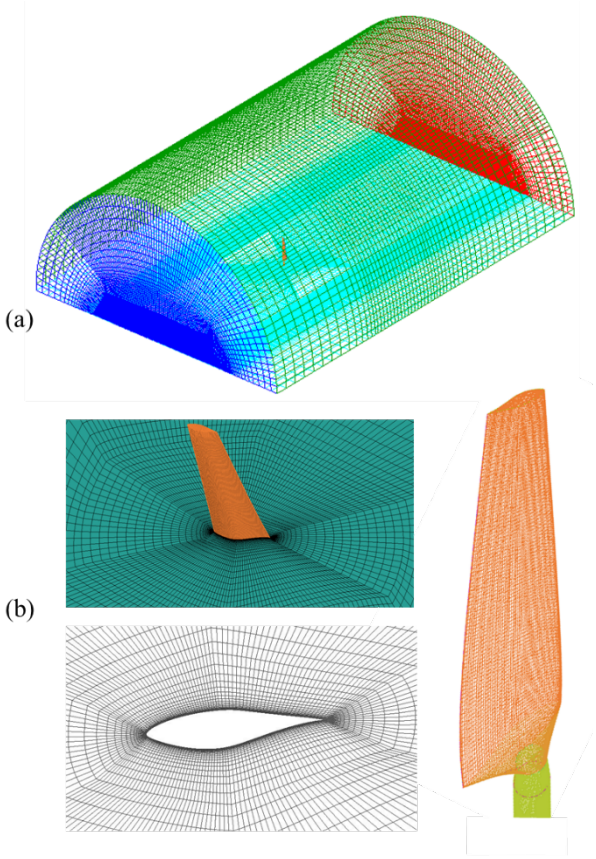

Fig 5. Computational mesh. (a) Complete domain; and (b) blade surface and cross section mesh

The production terms are:

$$P_k = \mu_t \left(\frac{\partial U_i}{\partial x_j} + \frac{\partial U_j}{\partial x_i} \right) \frac{\partial U_i}{\partial x_j} \tag{4}$$

$$\tilde{P}_k = \min\left(P_k, 10\beta^* \rho k\omega \right) \tag{5}$$

The blending function F_1 is given by:

$$F_1 = \tanh\left\{ \left(\min\left[\max\left(\frac{\sqrt{k}}{\beta^* \omega y}, \frac{500\mu}{\rho y^2 \omega} \right), \frac{4\rho\sigma_{\omega 2} k}{CD_{k\omega} y^2} \right] \right)^4 \right\} \tag{6}$$

$$CD_{k\omega} = \max\left(2\rho\sigma_{\omega 2} \frac{1}{\omega} \frac{\partial k}{\partial x_j} \frac{\partial \omega}{\partial x_j}; 10^{-10} \right) \tag{7}$$

where:

- k is the turbulence kinetic energy,
- ω is the turbulent dissipation frequency,
- y is the normal distance to the nearest wall,
- U is the flow velocity,
- ρ is the density,
- μ is the dynamic viscosity

The turbulent eddy viscosity (μ_t) is given by:

$$\mu_t = \frac{a_1 \rho k}{\max(a_1 \omega; SF_2)} \tag{8}$$

where $S = \sqrt{2S_{ij}S_{ij}}$ is the invariant measure of the strain rate, and a_1 is a constant. The value of $a_1 = 0.30$ is used in present work, instead of $a_1 = 0.31$. The blending function F_2 is given by:

$$F_2 = \tanh\left\{ \left[\max\left(\frac{2\sqrt{k}}{\beta^* \omega y}, \frac{500\mu}{\rho y^2 \omega} \right) \right]^2 \right\} \tag{9}$$

F_1 and F_2 are blending functions which are designed to be one inside the boundary layer (k-ω model), and switches over to zero for free shear layers (k-ε model).

All constants in the SST model are calculated by a blend from the corresponding constants of the k-ω and the k-ε model via:

$$\varphi = \varphi_1 F_1 + \varphi_2 (1 - F_1) \; ; \qquad \varphi = \{\sigma_k, \sigma_\omega, \beta, \alpha\} \tag{10}$$

The constants for this model are:

$$\sigma_{k1} = 0.85, \; \sigma_{\omega 1} = 0.5, \; \beta_1 = 0.075, \; \alpha_1 = 5/9,$$
$$\beta^* = 0.09, \; \sigma_{k2} = 1.0, \; \sigma_{\omega 2} = 0.856, \; \beta_2 = 0.0828,$$
$$\alpha_2 = 0.440$$

3. Results and discussion

3.1 Numerical validation

The validation of CFD was performed by comparing the simulation results with the baseline blade (i.e., NREL Phase VI) experimental data (Simms et al. 2001; Hand et al. 2001).

As shown in Fig.6, the predicted rotor power and axial thrust values are generally in good agreements with the experimental results. Although, there is a slight overprediction of the rotor power at 11 m/s wind speed, and an underprediction of the rotor power for high wind speeds of 15-20 m/s where massive flow separations occur. The computed rotor power value at 17 m/s wind speed is approximately 18% low compared to measured data.

Figure 7 presents comparisons of predicted and measured pressure coefficient distributions on the blade's five spanwise sections (0.30, 0.47, 0.63, 0.80 and 0.95R) for the case of 7 m/s, 10 m/s, 15 m/s, and 20 m/s wind speeds. The pressure coefficient (C_p) is obtained by Equation (11), where P_∞ is the free stream pressure, Ω is the rotational speed of the blade, U_∞ is the free stream wind speed, and r is radius of section.

$$C_p = \frac{p - p_\infty}{0.5\rho \left(U_\infty^2 + (\Omega r)^2 \right)} \tag{11}$$

At low wind speed (7 m/s), the predicted pressure coefficient distributions at all sections of the blade agree well with the measured values.

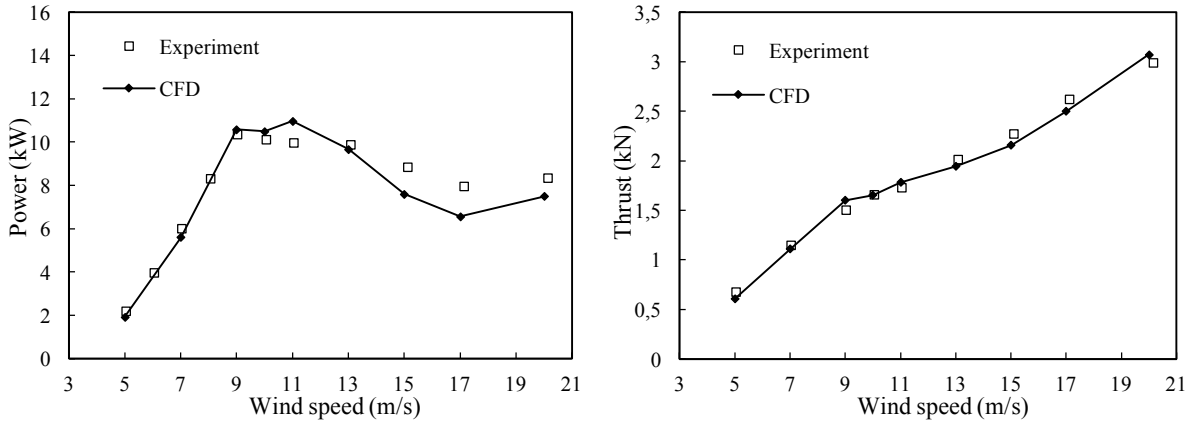

Fig 6. The calculated rotor power and thrust of the baseline blade

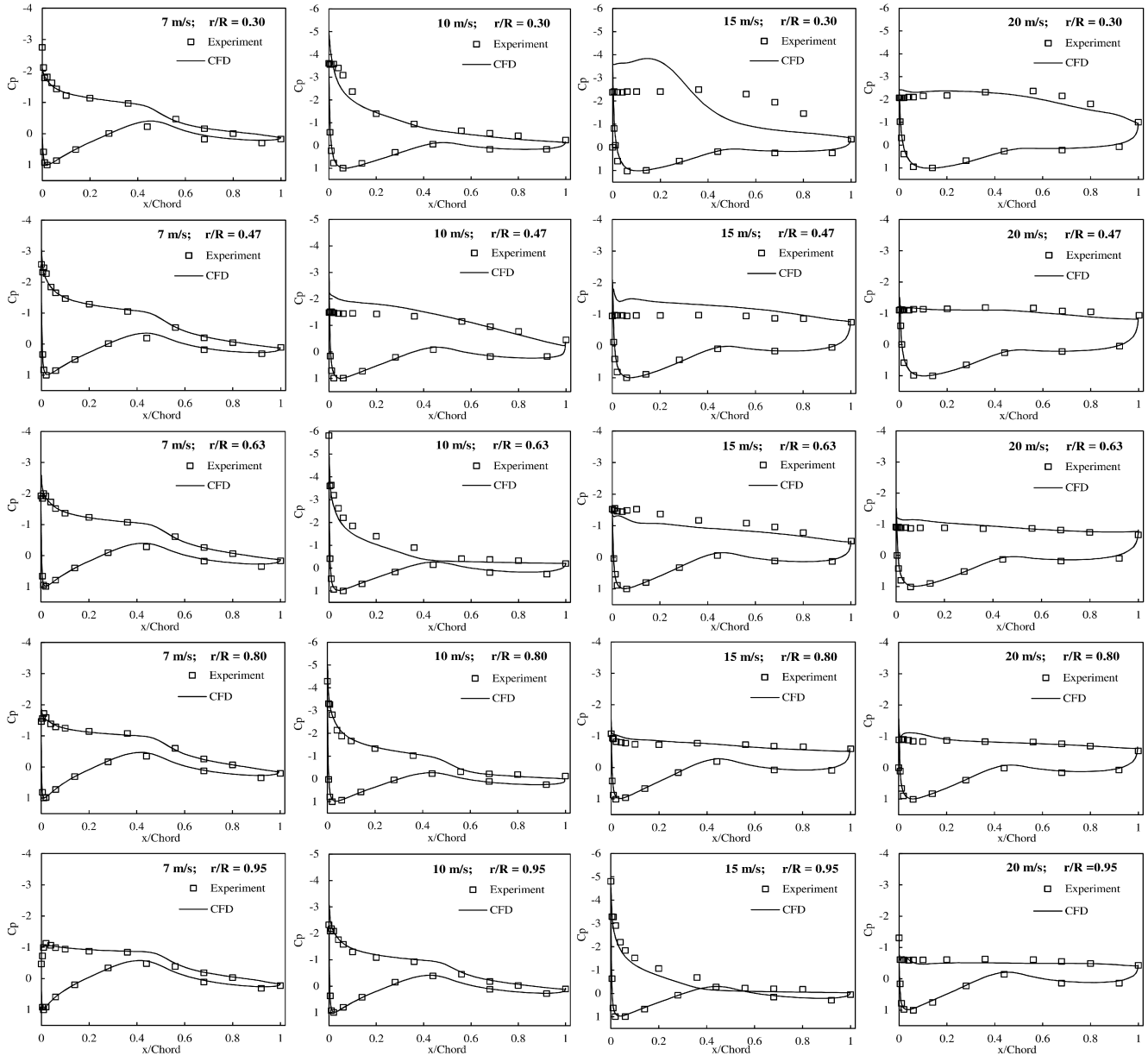

Fig 7. Comparison of measured and computed pressure distributions at 7 m/s, 10 m/s, 15 m/s and 20 m/s wind speeds

In the case of 10 m/s, there is a slight difference between the predicted and measured pressure distributions on the suction side for x/c < 0.4 at the span sections r/R = 0.30, 0.47 and 0.63. At 15 m/s wind speed, a large discrepancy in pressure distributions is noticed at r/R=0.30 section, which is believed to be due to the large separation and strong vortices due to high blade twist near the root. At 20 m/s wind speed, where the flow is fully separated over the entire blade span, the computed pressure distributions regain good agreements with the experimental results since the effects of the turbulence model are no longer influential.

3.2 Power and thrust

In this section, comparisons of CFD simulation results of the baseline blade and the twist modified blades are presented. The rotor power and thrust comparisons and their percentage changes from the baseline blade are shown in Fig.8 and Fig.9, respectively.

From Figure 8, the power captures of TW1, TW3 and TW5 blades (i.e., the cases that increase the twist angles from the baseline twist distribution) are less than the baseline blade at low wind speeds and become higher than the baseline blade at medium and high wind speeds. Compared with the baseline case, the TW1 blade has the maximum increase in rotor power around 11.2% at 10 m/s wind speed, the TW3 blade has the maximum increase in rotor power about 27% at 13 m/s, and the TW5 blade has the maximum percentage increase in rotor power about 50.9% at the wind speed 15 m/s. For the TW2, TW4 and TW6 blades (i.e., the cases that decrease the twist angles), the opposite is true wherein the power captures are lower than the baseline blade at medium and high wind speeds but are higher than the baseline blade at low wind speeds. Compared to the baseline blade, the rotor power of TW2 blade is reduced around 17.5% at the wind speed 9 m/s, and TW6 blade has the maximum percentage decrease in rotor power about 26.4% at 13 m/s.

Figure 9 shows axial thrust comparisons. In contrast to the rotor power curves, there are small difference in the thrust among the blades when wind speed is higher than 9 m/s. In comparison with the baseline blade, TW1, TW3 and TW5 blades exhibit lower thrusts at low wind speeds and slightly higher at medium and high wind speeds with maximum percentage increase in thrust less than 2%. For the TW2 blade, the thrust as well as the power are quite lower than the baseline blade at 9 m/s wind speeds. This is due to the separated vortex on the suction surface of the blade.

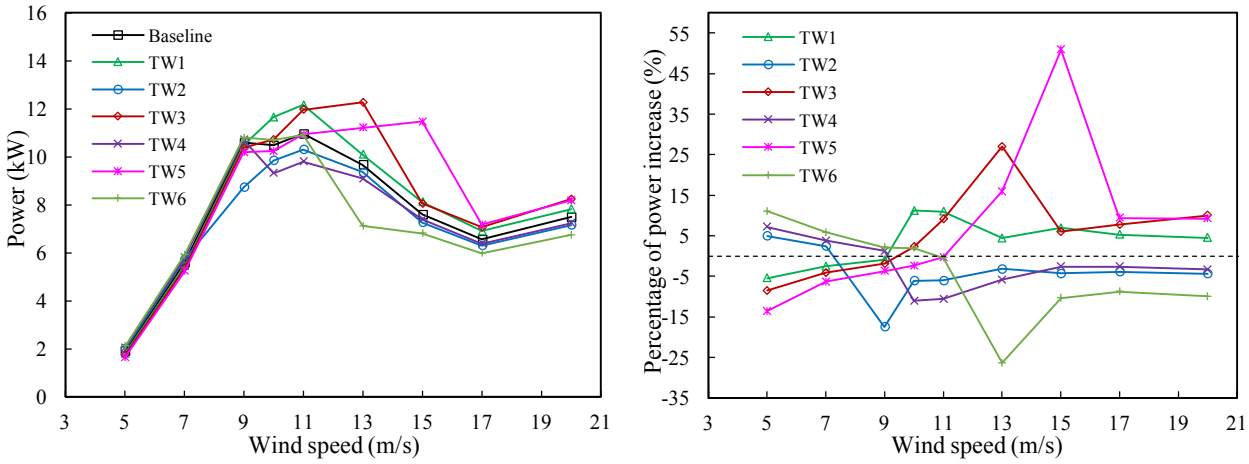

Fig 8. Comparison of rotor powers (left) and percentage changes from the baseline blade (right)

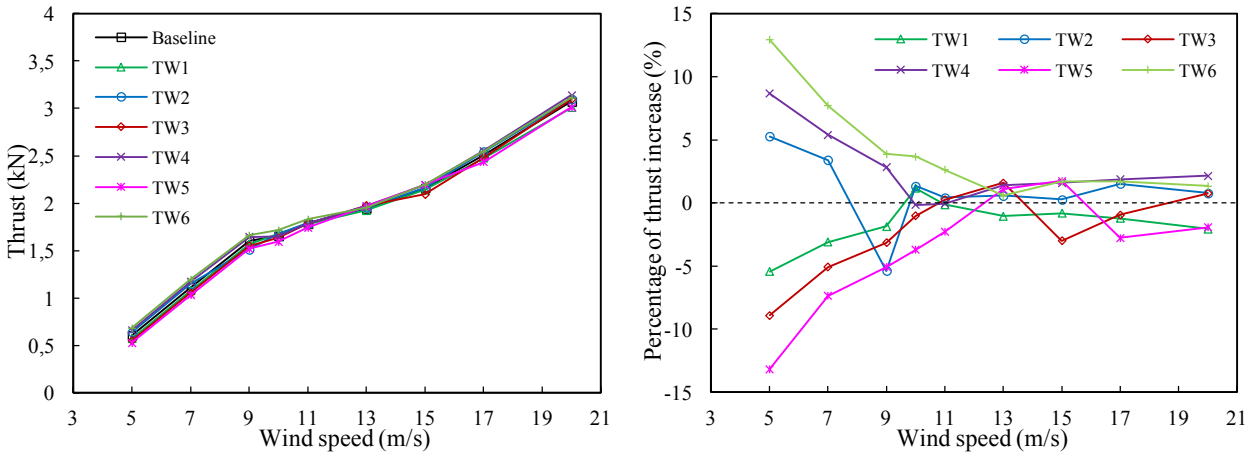

Fig 9. Comparison of axial thrusts (left) and percentage changes from the baseline blade (right)

3.3 Annual Energy Production (AEP)

AEP is a measure of economic feasibility of a wind turbine. To calculate AEP it is necessary to multiply the rotor power curve with the probability density function of the wind. In this study, Rayleigh wind speed distribution was used. For a given average (mean) wind speed $\bar{U}$, the probability of wind speed $f(U)$ is obtained by the following formulation:

$$f(U) = \frac{\pi}{2}\frac{U}{\bar{U}^2} exp\left(-\frac{\pi}{4}\left(\frac{U}{\bar{U}}\right)^2\right) \quad (12)$$

The annual mean wind speeds (AMWS) in the range of 6.2 to 8.2 m/s were used, which correspond to the average wind speed that used in designing the original rotor (Giguere and Selig 1999).

Figure 10 shows the Rayleigh wind speed distributions for three annual mean wind speeds; AMWS = 6.2 m/s, 7.2 m/s and 8.2 m/s. Figure 11 shows the distribution of annual mean wind power densities which are calculated from the Rayleigh distributions. The wind power density indicates how much wind energy is available at a site. From Figure11, it is noticed that the highest wind power densities are found at wind speeds around 10 m/s, 11.5 m/s, and 13 m/s for annual mean wind speed 6.2 m/s, 7.2 m/s, and 8.2 m/s, respectively.

Figure 12 and Table 1 show the percentage increases in annual energy production (AEP) of the modified blades compared with the baseline blade. It can be seen that TW1 and TW3 blades can produce higher AEP than the baseline blade for all annual mean wind speeds from 6.2 to 8.2 m/s. Comparison to the baseline blade, the AEP of blades TW1 and TW3 increase by 2.4% to 3.9% and 1.8% to 5.1%, respectively. This is mainly due to the blades having high percentage of rotor power increases at wind speeds in the range of 10-13 m/s which contain high wind power densities. The TW5 blade tends to produce higher AEP than the baseline blade at high annual mean wind speeds, due to the blade having higher rotor power than the baseline blade at high wind speeds. In the cases of TW2, TW4, and TW6 blades, their AEPs are lower than the baseline blade at all annual mean wind speeds, except at AMWS = 6.2 m/s for the TW6 blade.

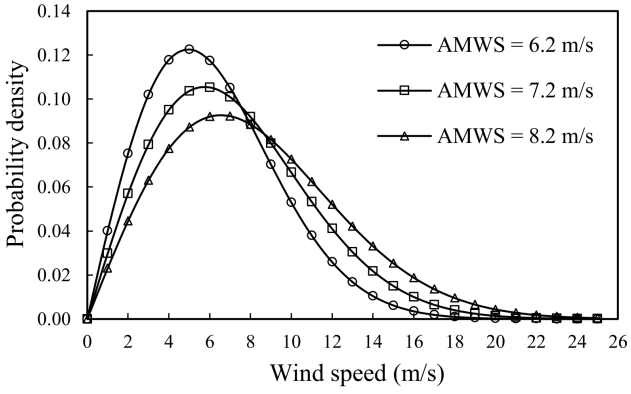

Fig 10. Rayleigh distributions for annual mean wind speeds of 6.2, 7.2 and 8.2 m/s

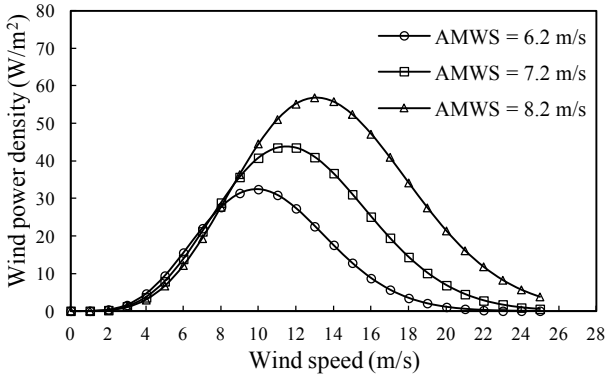

Fig 11. Wind power densities for the mean wind speeds of 6.2, 7.2 and 8.2 m/s

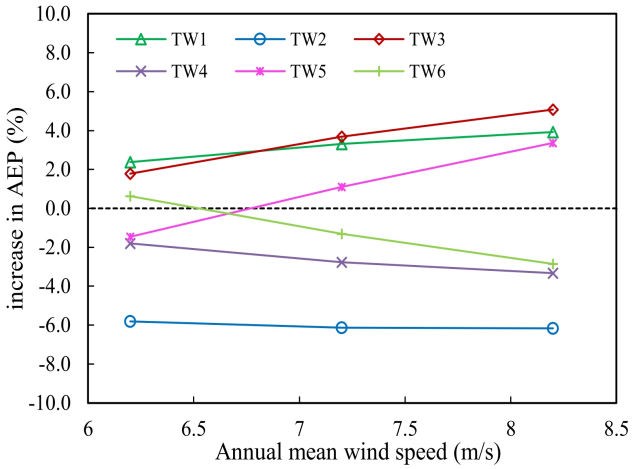

Fig 12. Increase/decrease in AEP compared to the baseline blade

4. Conclusion

In this paper, the effects of blade twist modifications of the NREL Phase VI wind turbine were studied using CFD. The validation results for the baseline blade obtained using RANS with the *k*-ω SST turbulence closure model were generally in good agreement with the experimental data, though discrepancy existed at high wind speed conditions. The baseline blade was modified by increasing or decreasing the twist angles in the inboard, mid-board and outboard regions of the blade in the form of a symmetrical curve. The results show that the rotor power of the increasing blade twist cases have significant improvements over the baseline values under medium and high wind speed conditions, while those of the decreasing blade twist cases have little improvements under low wind speeds. For annual mean wind speeds in the range of 6.2 to 8.2 m/s, it is found that the cases of increasing twist angles at blade regions 0.30-0.60R (TW1 blade), and 0.45-0.75R (TW3 blade) show best results with increase of AEP by 2.4% to 3.9% and 1.8% to 5.1%, respectively. This study thus has confirmed that, under proper design, the blade twist modification in conjunction with 3D stall delay phenomenon can help improves efficiency of wind turbine rotor.

Table 1
Annual Energy Production Comparison

AMWS (m/s)	Baseline blade	TW1 blade		TW2 blade		TW3 blade	
	AEP (MWh/y)	AEP (MWh/y)	Increase rate (%)	AEP (MWh/y)	Increase rate (%)	AEP (MWh/y)	Increase rate (%)
6.2	36.435	37.301	2.375	34.316	-5.816	37.087	1.789
7.2	44.775	46.260	3.317	42.031	-6.129	46.428	3.692
8.2	50.431	52.408	3.921	47.321	-6.165	52.996	5.087
AMWS (m/s)	**Baseline blade**	**TW4 blade**		**TW5 blade**		**TW6 blade**	
	AEP (MWh/y)	AEP (MWh/y)	Increase rate (%)	AEP (MWh/y)	Increase rate (%)	AEP (MWh/y)	Increase rate (%)
6.2	36.435	35.776	-1.810	35.904	-1.457	36.667	0.636
7.2	44.775	43.534	-2.771	45.267	1.100	44.189	-1.308
8.2	50.431	48.750	-3.333	52.125	3.360	48.989	-2.859

Acknowledgments

This research is supported by the Royal Golden Jubilee Ph.D. Program of the Thailand Research Fund.

References

Ahmadi MH, Ghazvini M, Sadeghzadeh M, et al. (2018) Solar power technology for electricity generation: a critical review. *Energy Sci Eng*. 6(5), 340-361.

Ahmadi MH, Alhuyi Nazari M, Ghasempour R, Pourfayaz F, Rahimzadeh M, Ming T. (2018) A review on solar-assisted gas turbines. *Energy Sci Eng*. 6(6):658–74.

Ahmadi MH, Ramezanizadeh M, Nazari MA, Lorenzini G, Kumar R, Jilte R. (2018). Applications of nanofluids in geothermal: A review. *Mathematical Modelling of Engineering Problems*. 5(4), 281-5.

ANSYS FLUENT 12.1 (2009) *User's Guide*, Fluent Inc.

ANSYS ICEM CFD 12.1 (2009) *User Manual*, Fluent Inc.

Chow, R. & van Dam, C.P. (2012) Computational investigations of blunt trailing-edge and twist modifications to the inboard region of the NREL 5 MW rotor. *Wind Energy*, 16, 445–458.

Duque, E.P.N., Burklund, M. D., & Johnson, W. (2003) Navier-stokes and comprehensive analysis performance predictions of the NREL phase VI experiment. *Journal of Solar Energy Engineering*, 125, 457-467

Giguere, P. & Selig, M. (1999) Design of a tapered and twisted blade for the NREL combined experiment rotor. *NREL/SR*. 500-26173.

Guntur, S. (2013) *A Detailed Study of the Rotational Augmentation and Dynamic Stall Phenomena for Wind Turbines*. PhD thesis, DTU Vindenergi.

Hand, M.M., Simms, D.A., Fingersh, L.J., Jager, D.W., Cotrell, J.R., Schreck, S. & Larwood, S.M. (2001) Unsteady aerodynamics experiment phase VI: wind tunnel test configurations and available data campaigns. *NREL/TP*-500-29955.

Hansen, O.L., Sorensen, J.N., Voutsinas, S., Sorensen, N., & Madsen, H.Aa. (2006) State of the art in wind turbine aerodynamics and aeroelasticity. *Prog. Aerosp. Sci*. 42, 285–330.

Himmelskamp H. (1947) Profile investigations on a rotating airscrew. Reports and translations, MAP Völenrode: Göttingen, Germany.

Hsu, M.C., Akkerman, I., & Bazilevs, Y. (2013) Finite element simulation of wind turbine aerodynamics: validation study using NREL Phase VI experiment. *Wind Energy*, 17(3), 461–481.

Johansen, J., Sørensen, N. N., Michelsen, J. A., & Schreck, S. (2002) Detached-Eddy Simulation of Flow around the NREL Phase-VI Rotor. *Wind Energy*, Vol. 5, No. 2-3, 185-197

Li, Y., Paik, K.J., Xing, T. & Carrica, P.M. (2012) Dynamic overset CFD simulations of wind turbine aerodynamics. *Renewable Energy*, 37,285–298.

Menter, F.R. Kuntz, M. & Langtry, R. (2003) Ten Years of Industrial Experience with the SST Turbulence Model. *Heat and Mass Transfer*, 4, 625–632.

Ramezanizadeh M, Nazari MA, Ahmadi MH, Lorenzini G, Kumar R, Jilte R. (2018). A review on the solar applications of thermosyphons. *Mathematical Modelling of Engineering Problems*. 5(4): 275-280.

Schreck, S., Robinson, M. (2002) Rotational augmentation of horizontal axis wind turbine blade aerodynamic response. *Wind Energy*, 5, 133–150.

Simms, D., Schreck, S., Hand, M., Fingersch, L.J. (2001) NREL Unsteady Aerodynamics Experiment in the NASA-Ames Wind Tunnel: A Comparison of Predictions to Measurements. Technical Report; National Renewable Energy Laboratory (NREL): Golden, CO, USA.

Sørensen, N.N., Michelsen, J.A., & Schreck, S. (2002) Navier-Stokes Prediction of the NREL Phase VI Rotor in the NASA Ames 80 ft x 120 ft Wind Tunnel. *Wind Energy*, 5,151-169.

Thumthae, C., & Chitsomboon, T., (2007) Appropriate Domain Size for Numerical Simulation of Horizontal-Axis Wind Turbines. The 21 st Conference of Mechanical Engineering Network of Thailand, Chonburi.

Wood, DH. (1991). A three-dimensional analysis of stall-delay on a horizontal-axis wind turbine. *Journal of Wind Engineering and Industrial Aerodynamics*, 37,1-14.